Low-Cost Adaptive Array Demodulation of Bragg-Grating and Interferometric Sensors for Health Monitoring of Marine Structures

Final Report

Contract No: N00014-04-1-0052

Submitted by

Sridhar Krishnaswamy, Yi Qiao, Yi Zhou

CENTER FOR QUALITY ENGINEERING AND FAILURE PREVENTION
NORTHWESTERN UNIVERSITY
EVANSTON, IL 60208-3020

20060403305

Table of Contents

1. Introduction

Fiber Bragg Grating (FBG) sensors are an increasingly important emerging technology in the area of intelligent structural health monitoring (SHM) of civil, mechanical, naval and aerospace structures.[1-9] A large number of FBG sensors can be easily written in a single fiber. For SHM applications, FBG sensors are typically used to monitor static or dynamic strains. The strains cause spectral shifts in the FBG sensor transmittivity (equivalently reflectivity). The spectral shifts can be monitored in several ways with an appropriate demodulator. For spectrally-encoded FBG sensors, extant demodulation schemes can be classified into three categories, namely: scanning type, spectrometry-based and interferometry-based. Scanning type techniques include Fabry-Perot scanning filters,[10] acousto-optic tunable filters,[11] and tunable laser sources.[12-13] All these scanning type techniques suffer from the fact that at any instant only one FBG sensor can be interrogated. Such approaches are not applicable if all the sensors have to be interrogated *simultaneously* for the purpose of monitoring impact signals and acoustic emissions.[14] Spectrometric methods[15] suffer from low sensitivity and are not suitable for dynamic measurements if several sensors have to be active at all times. Interferometric methods such as the Mach-Zehnder interferometer[16] are ideally-suited to monitor dynamic strains; however they require electronic feedback to actively compensate for any quasistatic drift to maintain the interferometer at quadrature. This makes the cost of multiplexing high since each sensor requires its own feedback system. A cost-effective and parallel demodulation scheme for arrays of FBG sensors is therefore necessary.

In work over the past two years, we have demonstrated a novel two-wave mixing (TWM) wavelength demodulation scheme for FBG sensors that has the ability to compensate for quasistatic drifts without the need for active stabilization. This method is suitable for measuring dynamic and transient strains such as those induced by vibrations, impact, ultrasound, or acoustic emission. Furthermore, this scheme can be readily multiplexed by using wavelength division multiplexing. Thus far, a four-channel TWM device has been demonstrated to demodulate dynamic strain signals from four FBG sensors simultaneously.

In Section II, the details of accomplishments to date are given. In section III, a plan of work for continued research is outlined. The aim of the continuation phase is to scale up the system developed so far and to demonstrate application on a real structure with a view to transitioning the technology.

II. Work to Date:

2.1 Adaptive Two-wave Mixing Photorefractive two-wave mixing is essentially a dynamic holographic process where two coherent optical beams, typically one stronger pump beam and one weaker signal beam, interact within a photorefractive crystal (PRC).[17-18] The process can be briefly summarized as: (1) creation of intensity gratings due to coherent stationary interference of the interacting beams leading to (2) non-uniform photo-excitation of charges in the PRC which then diffuse/drift to create (3) a space-charge field within the PRC, which in turn creates (4) a refractive index grating via the electro-optical effect, and which causes (5) diffraction of the interacting beams. This process of dynamic coupling is known as wave mixing, a

phenomenon that has been exploited over the years for a variety of applications[17-18] including in optical interferometry.[19-24]

Figure 1 shows a schematic of a simple TWM interferometer in the so-called direct detection configuration[21] used in this paper. The signal beam and pump beam interfere with each other inside the PRC and create an index grating in the PRC. A part of the pump beam is diffracted by the created index grating into the direction of the transmitted signal beam. The diffracted pump beam is wavefront-matched with the quasistatic signal beam. Subsequent to the PRC, the diffracted pump beam and the transmitted signal beam interfere with each other to demodulate any phase difference between them. The TWM interferometer is adaptive because the created index grating is a dynamic grating and the crystal can adapt to any phase shift that is slower than the PRC response time by forming a new index grating. The diffracted pump beam will therefore track any quasistatic changes in the signal beam phase, resulting in no net quasistatic phase difference between the diffracted pump and transmitted signal beams. Only dynamic phase changes faster than the photorefractive response time of the PRC will not be present in the diffracted pump beam. This will result in a net phase difference between the diffracted pump and the transmitted signal beams subsequent to the PRC, which can then be picked up by interference of these two beams. By application of an external DC field to the PRC (the so-called drift regime), the interference pattern can be kept nearly in phase with the created index grating.[25] in the drift regime, by adjustment of the applied field and two beam mixing angle, the TWM interferometer can be made to work at near quadrature (that is, the diffracted pump beam is nearly $\pi/2$ phase shifted with respect to the transmitted signal beam) for sensitive and linear interferometric detection. The adaptivity of the TWM process in the PRC implies that the system will *remain* at quadrature without any need for active external stabilization despite quasistatic drifts that may occur. The PRC can therefore be regarded as an adaptive high-pass filter that selectively monitors any high frequency changes in the mixing beams. This is ideal for monitoring small dynamic strain signals (such as those induced by impact or acoustic emissions) that may ride on top of large quasistatic drifts (caused by static stressing or temperature). It should also be noted that the TWM interferometer is readily multiplexable using any combination of angular multiplexing, spatial multiplexing or wavelength multiplexing. This enables multiple interferometers to be configured in one simple device.[26-28]
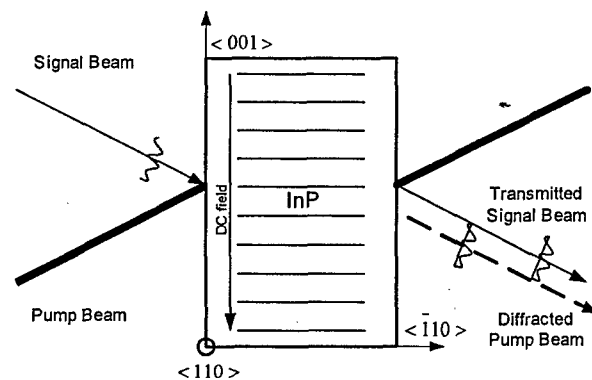

Figure 1 Schematic of the TWM direct detection setup

Following the analysis of Delaye et al[21], the amplitude of the transmitted signal beam subsequent to the PRC can be denoted as:

$$Es = E_0 \exp[i\phi(t)] \qquad (1)$$

Here $\phi(t)$ is the dynamic phase-shift which is the signal of interest. E_o is the complex amplitude of the signal beam and may include an additional phase term φ_n to account for quasistatic phase shifts due to noise. The amplitude of the diffracted pump beam E_{dp} can then be written as a function of the TWM gain as follows:[21]

$$E_{dp} = E_0\{\exp[\gamma L] - 1\}, \qquad (2)$$

in which $\gamma = \gamma' + i\gamma''$ is the TWM complex gain and l is the crystal length in the beam propagation direction. It is the interference between the diffracted pump e_{dp} and the transmitted signal beam e_s that demodulates the spectral shift $\Delta\lambda_B$. In the limit of small dynamic phase shifts (this is usually valid for the dynamic strains induced by acoustic emission or impact, for instance), the interference signal at the photodetector can be written as:

$$I = |E_o|^2 \left\{ e^{2\gamma'L} + 2\sin(\gamma''L)e^{\gamma'L} \; \varphi(t) \right\} \qquad (3)$$

The first term in the curly brackets represents a dc level and contributes to photodetector shot noise. The second term represents the signal of interest, and indicates that the interference signal varies linearly with the dynamic phase shift (for small phase shifts) between the signal and pump beams. It is clear from eq. (3) that the maximum signal occurs when $\gamma''L$ approaches $\pi/2$, that is at quadrature. This condition can be readily approached in the drift regime by application of an electric field to the PRC, and by appropriately adjusting the TWM parameters.

2.2 Adaptive Two-wave Mixing Wavelength Demodulator

We now show that the TWM interferometer can be configured as a *wavelength* demodulator for FBG sensors. The light reflected from an FBG sensor is first split into two beams, one pump and one signal beam, which are made to travel *unequal* paths prior to mixing in the PRC. Any wavelength shift of the light reflected from the FBG sensor then results in an equivalent *phase* shift between the pump and signal beams because of travel over unequal optical paths. Therefore, in the sense of converting a wavelength shift of the FBG sensor signal into an equivalent phase shift, the underlying principle used here is the same as that used in Mach Zehnder Interferometry and other unbalanced-path interferometric methods.[16]

The spectral shift induced by strain and temperature in a Bragg-grating sensor can be written as:[29]

$$\frac{\Delta\lambda_B}{\lambda_B} = [1 - \frac{n_{eff}^2}{2}[p_{12} - \upsilon(p_{11} + p_{12})]]\varepsilon_z + (\alpha_\Lambda + \alpha_N)\Delta T, \qquad (4)$$

in which λ_B is the center wavelength of the FBG sensor, $\Delta\lambda_B$ is the wavelength shift caused by strain or temperature, n_{eff} is the effective refractive index of the fiber, p_{ij} are the components of the strain-optic tensor, υ is Poisson's ratio, ε_z is the strain along the fiber, α_Λ is the thermal expansion coefficient and α_n is the thermo-optic coefficient of the fiber. For typical Bragg-sensors at 1550nm, it has been estimated that one micro-strain ($1\mu\varepsilon$

$=10^{-6}$) will lead to a ~1.2 pm change in wavelength, and a 1°C change in temperature will lead to about 13pm change in wavelength.[29]

As mentioned earlier, a spectral shift $\Delta\lambda_B$ of the signal *and* pump beams is effectively converted into a relative phase shift *between* the beams (due to travel through unbalanced optical paths), and this is given by:[29]

$$\phi(t) = \frac{2\pi d}{\lambda_B^2}\Delta\lambda_B, \qquad (5)$$

where d is the optical path difference (OPD), λ_B is the center wavelength of the FBG sensor, $\Delta\lambda_B$ is the wavelength shift of the light reflected by the FBG. From Eq(5), it appears that the greater the OPD, the larger the equivalent phase shift, and therefore the stronger the interference signal should be. However, typically broadband light sources are used to illuminate the FBG sensors, and the FBG reflection spectrum typically has a finite line width on the order of 0.1-0.4nm. This implies that coherence of the two interfering beams needs to be taken into account both in the photorefractive grating creating process and in the subsequent interference between the transmitted signal and the diffracted pump beams. The fringe visibility due to interference of two beams of finite spectral width Δk is given by:

$$V = \frac{2\sqrt{r}}{r+1} \times \exp(-\frac{\Delta k^2 d^2}{16\ln 2}) \qquad (6)$$

where r is the intensity ratio of the two beams, and d is the OPD. Incorporating the degradation in fringe visibility due to low coherence in the TWM analysis leads to a modified expression for Eqn(3). The TWM spectral-shift demodulated interference signal (neglecting the dc-component for simplicity) can be shown to be proportional to:

$$S \propto \exp(\gamma' L)\sin(\gamma'' L)\exp(-\frac{\Delta k^2 d^2}{16\ln 2})\frac{d\,\Delta\lambda_B}{\lambda_B^2} \qquad (7)$$

The effect of decreased fringe visibility on the photorefractive grating formation process is not a significant factor, since the preferred mode of two-wave mixing in PRCs is in the low intensity modulation regime (this avoids the creation of higher order index gratings leading to multiple diffracted beams). Furthermore, the system is operated at near quadrature, $\gamma'' L \approx \pi/2$, and since the TWM energy gain (the real part of the complex gain) is typically very small, the variations in the first two terms with the OPD are not significant (as will be demonstrated in the experimental section). The dependence of the interference signal on the OPD is therefore predominantly given by:

$$S \propto \exp\left\{-\frac{\Delta k^2 d^2}{16\ln 2}\right\}\frac{d\,\Delta\lambda_B}{\lambda_B^2} \qquad (8)$$

The wavelength demodulation signal is therefore a strong function of the OPD d with the exponential decay arising from loss of coherence, and the linear increase arising from the increase with OPD in the phase-shift due to spectral change. Figure 2 is a plot of the signal amplitude versus the OPD for different line-width FBG sensors. (In the calculation of Figure 2, L was set equal to 1cm and a value of 0.3 cm^{-1} for was used for the real part of the TWM complex gain). As indicated in Figure 2, when the OPD equals zero, there is no wavelength-demodulated signal detected, and as the OPD increases the signal amplitude increases to a maximum beyond which the signal starts to drop due to

6

decreasing fringe visibility. For each given line width of the FBG sensor, there exists an optimum value of the OPD that maximizes the wavelength-demodulated signal. It is also clear from Figure 2 that the narrower the line width, the larger the optimum OPD and therefore the larger the demodulated signal. However, it is not always better to use a narrower line-width FBG sensor. First, a narrower line-width FBG sensor is usually longer in length,[29] which decreases the highest frequency to which the FBG can respond.[30] Secondly, a larger OPD decreases the dynamic range that the FBG sensor can measure.
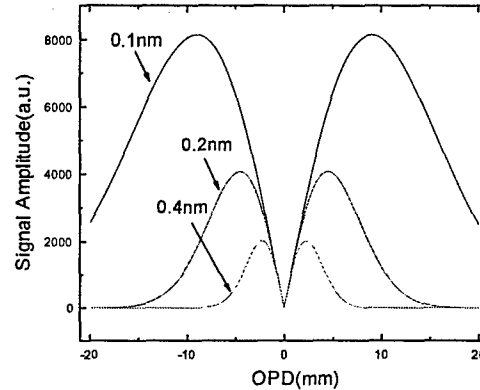

Figure 2 Wavelength demodulated signal amplitude as a function of the optical path difference (OPD) for different line-width FBG sensors.

2.3 Experimental Configuration The experimental configuration is shown in Figure 3. The FBG sensor is illuminated by a broadband amplified spontaneous emission (ASE) source in the C-band (1530nm to 1570nm), and the reflected light is coupled by a circulator into an Erbium doped fiber amplifier (EDFA) that works in saturation mode (output 500mW). The amplified light is split using a 1x2 coupler (splitting ratio 95/5) into pump (95%) and signal (5%) beams that travel unbalanced optical paths to the InP:Fe photorefractive crystal. The InP:Fe crystal is oriented for two-wave mixing in the direct detection configuration,[21] in which both beams enter the crystal by the [$\bar{1}$10] face. An external DC field is applied along <001> direction. In order to apply a continous DC field across the InP:Fe crystal, a peltier cooler is used to prevent electrical breakdown due to crystal overheating. (In some of the earlier experiments reported here, the peltier cooler had not been integrated into the set up, and in these cases the DC-field was applied intermittently to avoid possible damage to the crystal due to heating.) Two half-wave plates (HWP) are used prior to the PRC to rotate the pump and signal beam polarization to be s-polarized (along the <110> direction). Due to interference between the signal and pump beams, a refractive index grating forms in the PRC along the <001> direction. Under the applied external DC field (drift regime), the index grating is nearly in phase with respect to the interference pattern, and the diffracted pump and the transmitted signal beams are kept at near quadrature. This is optimal for demodulation of very small phase/wavelength changes.
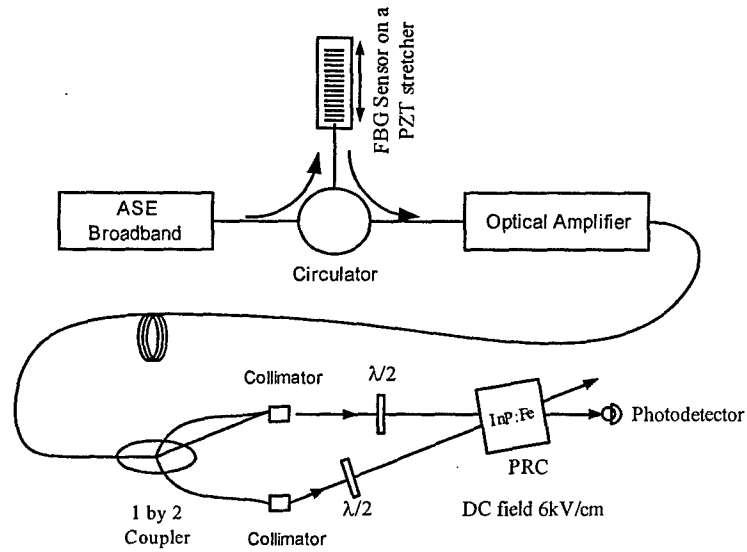
Figure 3 Experimental configuration of the FBG sensor and the two-wave mixing (TWM) wavelength demodulator.

2.4 Wavelength Demodulation In a first set of experiments, an FBG sensor centered at 1552nm with a line-width of 0.1nm, length of 10mm, and reflectivity of 50% was glued onto a PZT stretcher that was used to induce known dynamic strains. The light reflected from the FBG sensor undergoes spectral shift due to strain-induced changes in the Bragg-reflectivity. The sensor by itself is sensitive to both quasistatic and dynamic strains, and is also subject to temperature drift. However, as explained in the previous section, the TWM demodulator system will automatically compensate for quasistatic drifts and track only the dynamic strains.
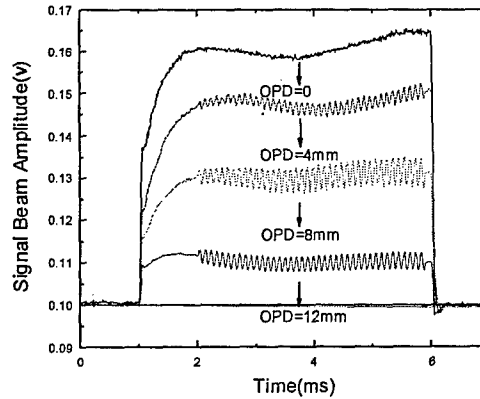

Figure 4 Wavelength demodulated signal at different values of OPD. An intermittent DC field is applied to the PRC starting from 1ms to 6ms and a 10 kHz 10 $\mu\varepsilon$ strain is applied to the FBG from 2ms to 6ms.

8

In order to demonstrate wavelength demodulation, we applied a 10 kHz, 10 με strain onto the FBG sensor and measured the wavelength demodulated signal amplitude at different values of the optical path difference. As shown in Figure 4, an intermittent DC field is applied from 1ms to 6ms with respect to a reference trigger, and the photorefractive grating initially builds up. The dynamic strain is applied as a toneburst starting from 2ms to 6ms.When the OPD equals to zero, although the TWM energy gain is at its maximum, there is no detected wavelength demodulated signal because there is no OPD to convert the wavelength shift into phase shift. As the OPD increases, the wavelength demodulated signal starts to appear.
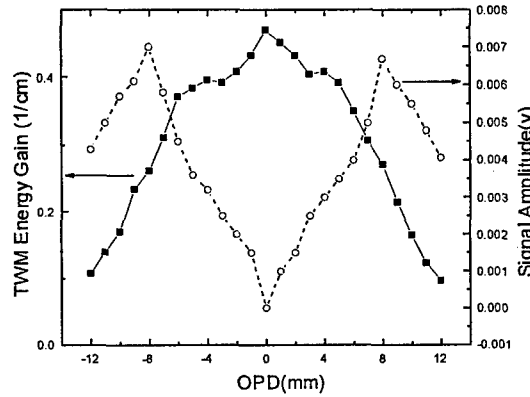

Figure 5 Plot of wavelength demodulated signal amplitude and TWM gain versus OPD.

Figure 5 is a plot of the wavelength demodulated signal amplitude and TWM energy gain versus the OPD. The optimum OPD that maximizes the wavelength demodulated signal for the 0.1nm line-width FBG sensor is found to be 8mm. For an OPD of 8mm, Eq. (5) indicates a wavelength-to-phase shift conversion sensitivity of about 21 radians per nanometer wavelength shift at 1550nm wavelength. This translates to 0.0252 radian/με. Such phase shifts are readily detectable by the TWM interferometer. Also note that the trend of the signal amplitude curve is similar to that of the theoretical curve shown in Figure 2. Also, as we mentioned in the theoretical section, the TWM energy gain γ' is indeed a small number and experimentally is found to vary from 0.47 cm^{-1} to 0.1 cm^{-1} as the OPD changes from 0 to 12mm. This causes the first exponential term in Eq.(7) to vary from 1.6 to 1.1, which is much smaller than the change in the second exponential term which decreases from 1 to 0.03 as the OPD increases from zero to 12mm.

The TWM demodulator output when operated at near quadrature is expected to be a linear function of the FBG spectral-shift (and hence strain). This is shown in Figure 6 where the demodulator output is plotted as a function of the dynamic (20 kHz) strain amplitude. The minimum detectable strain with our current setup was measured to be ~0.25με, corresponding to a spectral shift of 0.3pm. The minimum detectable spectral shift, which is limited by the ASE source and EDFA intensity noise, can be further improved by using balanced photodetection to cancel the intensity noise.
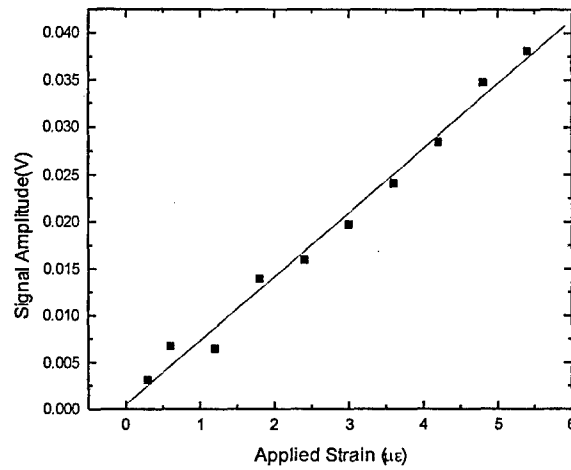
Figure 6 TWM demodulator output as a function of dynamic strain amplitude.

2.5 Adaptivity to Quasistatic Drift One of the advantages of using the two-wave mixing interferometer as a wavelength demodulator is its adaptivity to low frequency drift. As mentioned earlier, the two-wave mixing interferometer is automatically adaptive to low frequency strain or temperature drift of the FBG sensor. In order to demonstrate this feature, we subjected the FBG sensor to quasistatic strain and temperature drift, and tested the system response.
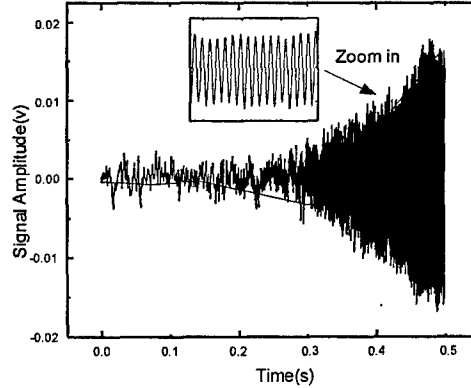

Figure 7 TWM wavelength demodulator response to a frequency sweep signal from 10 Hz to 1.2 kHz.
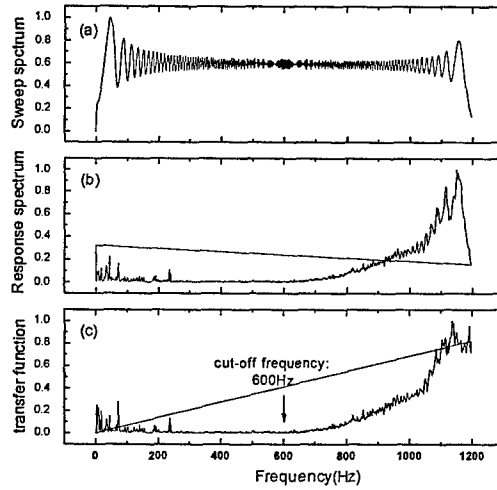
Figure 8 (a) Fourier spectrum of the applied frequency sweep signal from 10 Hz to 1.2 kHz. (b) Fourier spectrum of the response of the TWM wavelength demodulator. (c) Transfer function of the TWM wavelength demodulator. The cut-off frequency is seen to be around 600 Hz for this configuration.

In order to show adaptivity to quasistatic strain, we applied a frequency sweep signal from 10Hz to 1.2 kHz with a constant magnitude of $10\mu\varepsilon$. Figure 7 shows the response of the wavelength demodulator to this frequency sweep signal. The demodulator ignores the low frequency strain applied in the beginning and starts to respond to frequencies above 600Hz. Figure 8 demonstrates the adaptivity to quasistatic strain more clearly in the frequency domain. Figure 8 (a) is the Fourier spectrum of the applied sweep signal, Figure 8 (b) is the spectrum of the system response to the sweep signal, and Figure 8 (c) is the system transfer function (modulus) calculated by dividing the system response spectrum by the sweep signal spectrum.

From Figure 8, it is clear that the TWM wavelength demodulator is adaptive to low frequency strains and acts like a high pass filter with a cut-off frequency of 600 Hz. The cut-off frequency of the system is directly related to the response time of the InP:Fe PRC. The faster the PRC (shorter response time), the higher the cut-off frequency will be. Furthermore, the response time of the PRC can be tuned by adjusting the input optical intensity. Generally speaking, a higher optical intensity generates more photo-carriers inside the PRC, and the response is faster.[31] Note that the optical power density used here is $\sim$20mW/mm^2. Also, note that the low frequency peaks in the response spectrum are due to the output *intensity* fluctuations caused by the source, which however do not cause the demodulator to drift from quadrature, and are not of consequence here.

In principle, there is no upper limit arising from the TWM process for the detectable frequency range of the FBG spectral shift. The upper frequency is limited only by the FBG sensor response[30] and the electronics bandwidth of the photodetector circuit. As shown in Figure 9, a high frequency dynamic strain signal (a 580 kHz $3\mu\varepsilon$ strain applied to the FBG via a PZT-stretcher) is successfully demodulated by the TWM wavelength demodulator.
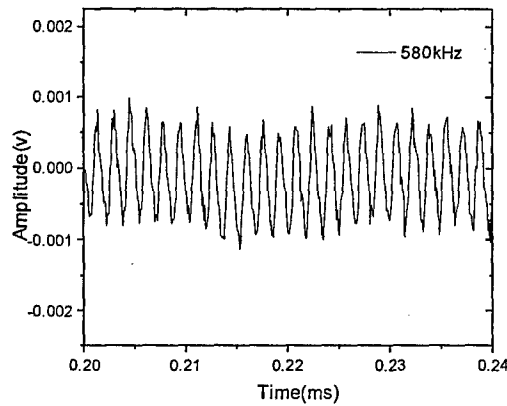
Figure 9 A 580 kHz 3με strain signal demodulated by the TWM wavelength demodulator.

Next we proceed to demonstrate that the system can also adapt to large temperature drifts. Temperature drift is introduced to the FBG sensor by using a thermo-electric cooler (TEC) module connected to a temperature controller, and the sensor temperature is monitored by a thermistor. A 0.1 Hz sine wave is used as input to the temperature controller and the temperature cycle amplitude is controlled by the sine wave amplitude. The temperature drift introduced here is a 10°C drift within 5 seconds (drift rate of 2°C/s which is extremely high). In order to verify that the temperature drift is effectively introduced to the FBG sensor, an ANDO (model 6317) optical spectrum analyzer is used to record the reflection spectrum of the FBG sensor as the temperature drift is introduced. As indicated in Figure 10, the temperature drift of 10°C causes a wavelength shift of 110pm, which is close to the expected shift of 130pm (13pm/°C).
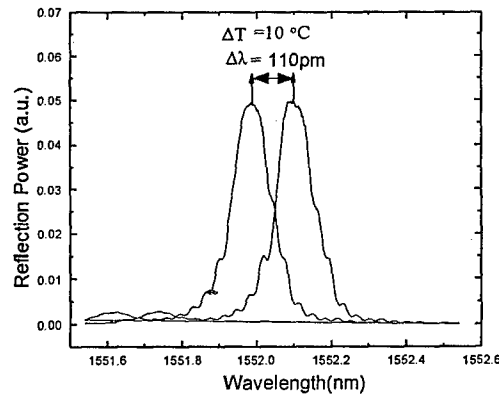

Figure 10 Reflection spectra of the FBG sensor subject to 10°C temperature drift. The center wavelength is shifted by 110pm due to the temperature drift.
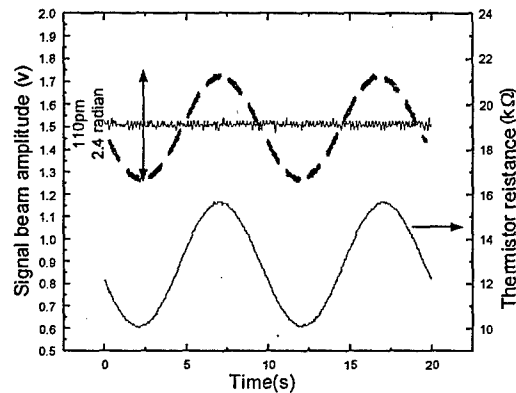
Figure 11 Time trace of the demodulator amplitude shows no variation due to the 0.1 Hz 10°C temperature cycling. The dashed curve is what the demodulator amplitude would look like if the PRC did not adapt to the 2.3 radian phase shift caused by the temperature drift. Also shown is the thermistor resistance which is a direct measure of the temperature change in the FBG.

Figure 11 is the time trace of the TWM demodulated signal, which shows no variation due to the 0.1 Hz 10°C temperature drift. When there is no DC field applied onto the InP:Fe PRC, the TWM demodulator signal amplitude was originally 1.2 volts. This increases to 1.5 volts due to the diffraction of pump beam when the DC field is applied. A 110pm wavelength shift will cause an equivalent phase shift of 2.3 radians for this configuration. If such a large phase shift were to be picked up by the system, the signal beam amplitude would undergo a large amplitude variation as indicated by the dashed curve in Figure 11. The fact that no such shift is observed indicates that the TWM demodulator adaptively compensates for the temperature drift. In practical applications, typical environmental temperature drifts will be on the order of a few degrees per hour, which is much slower than the case considered here (2°C/s). This demonstrates that the TWM wavelength demodulation system will be able to adapt to all reasonable environmental temperature drifts of FBG sensors.

2.6 Detection of transient impact signals Next we demonstrate the ability of the TWM wavelength demodulator to monitor transient (non-recurring) events such as acoustic emissions, vibrations and impact signals. This is possible because the TWM demodulator is always active (unlike scanned demodulation schemes). In this experiment, an FBG sensor was covered by a 1mm thick dry couplant made from silicon epoxy. A 3mm thick metal plate was placed on top of the couplant. A 3mm diameter ball bearing was dropped from about 5 cm above the metal plate. The oscilloscope used to capture the demodulated signals was triggered by the demodulated signal itself with a trigger level set to be slightly higher than the noise level. Figure 12 shows the time trace of the impact signal. The demodulated FBG sensor signal clearly shows multiple bouncing of the ball bearing. The frequency of the first impact signal is about 5 kHz.
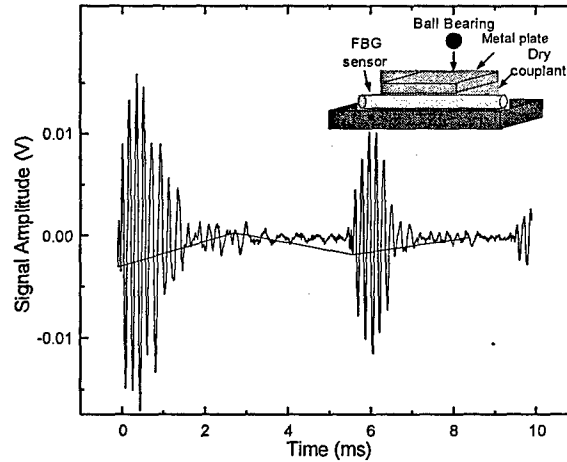
Figure 12 Time trace of the impact signal induced by dropping a ball bearing on a metal plate. The inset shows the experimental configuration of the impact event.

2.7 Four-channel Multiplexed TWM Demodulator In addition to adaptivity to low frequency drift, another major advantage of using TWM as wavelength demodulator for FBG sensors is that it can be multiplexed without significant increase in cost. This is because all the channels (wavelengths) share the same PRC and there is no expensive feedback electronics involved. Multiplexed TWM systems have been demonstrated previously at NU for phase-demodulation applications.[26-28] For FBG sensor demodulation, we adopt a simpler wavelength division multiplexing approach, in which all the channels share the same optical setup up to and including the PRC, and subsequent to wave mixing in the PRC these channels are separated by use of band-drop filters widely used in the optical communication industry.

Consider multiple FBG sensors with distinct spectral-reflectivities, with center wavelength separation $\Delta\lambda_c$ that is chosen to be sufficiently large so that stationary optical interference between the multiple channels cannot occur. In this case, inside the PRC each channel creates its own index grating of different grating pitches. The change in the index grating pitches is related to the channel separation and the signal and pump beam angles, and this can be shown to be:

$$\Delta\Lambda = \frac{\Delta\lambda_c}{2\sin(\theta/2)}, \quad (9)$$

in which $\Delta\Lambda$ is the change in index grating pitch, $\Delta\lambda_c$ is the channel separation and θ is the angle between the signal and pump beams. The FBG channel spacing $\Delta\lambda_c$ should be neither too small to avoid crosstalk involved due to closely packed index gratings, nor too large to maximize the number of sensors that can be used within the limited bandwidth of the C-band (1530-1570nm). In this work, the channel separation $\Delta\lambda c$ is chosen to be 4nm, which, according to Eq. (9), will give rise to an index grating pitch shift of 76nm at a beam angle of 3°. In the context of holographic storage elements using PRC's, it has been shown that multiple gratings can be written in a single PRC with negligible cross-talk if the grating pitches were to differ by as little as 0.03nm.[32] We therefore expect very small crosstalk in our setup, if any. Note that a 4nm channel spacing allows 10 channels

14

in the C-band. In practice, this can be increased by using narrower channel spacing, at the expense of decreased dynamic range.
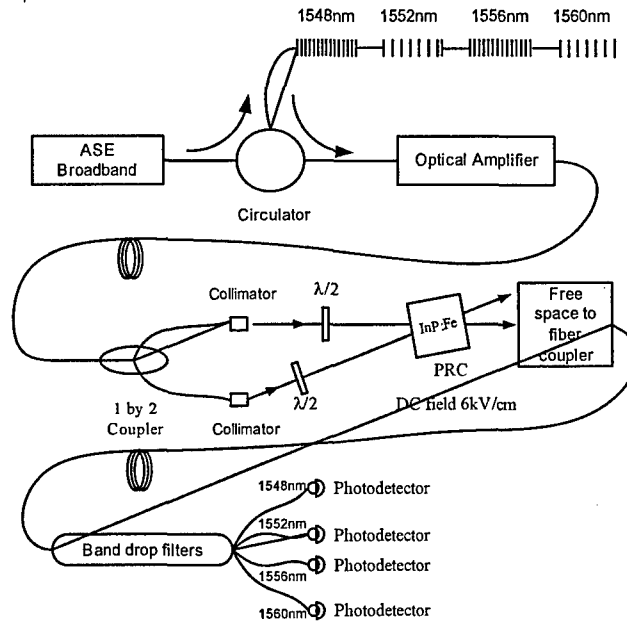
Figure 13 Experimental configuration of the four-channel two-wave mixing (TWM) wavelength demodulator.
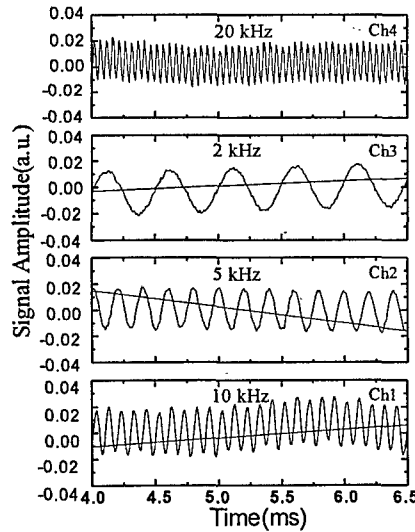

Figure 14 Simultaneous demodulation of the signals from four-FBG sensors using a 4-channel TWM wavelength demodulator. FBG sensor 1 (1548nm) is excited with 1 kHz 5 $\mu\varepsilon$ strain, sensor 2 (1552nm) 5 kHz 10 $\mu\varepsilon$ strain, sensor 3 (1556nm) 10 kHz 5 $\mu\varepsilon$ strain and sensor 4 (1550nm) 20 kHz 5 $\mu\varepsilon$ strain.

As a proof of concept, we now demonstrate a four-channel TWM wavelength demodulator. The experimental configuration is shown in Figure 13. Four 0.1nm linewidth FBG sensors are connected in series and are centered at 1548nm, 1552nm, 1556nm and 1560nm respectively. The experimental configuration is similar to that of the single channel configuration shown in Figure 3 except that after the PRC, there is a free space to fiber coupler to couple the free space light into a set of four band drop filters. A band drop filter is a three-port device that transmits a certain band (i.e. from 1546.8 nm to 1549.4nm) and reflects all the other wavelengths. The band drop filters therefore decouple the TWM demodulator signals from the various FBG sensors prior to photodetection. The width of the banddrop filter should be chosen to be wider than the expected quasistatic phase-shifts of the FBG sensors, and to be slightly narrower than the FBG channel spacing.

In order to establish the crosstalk of the four-channel system, we applied 10 kHz 5 $\mu\varepsilon$ strain on FBG sensor 1 (1548nm), 5 kHz 5 $\mu\varepsilon$ on FBG sensor 2 (1552nm), 2 kHz 5 $\mu\varepsilon$ on FBG sensor 3 (1556nm) and 20 kHz 5 $\mu\varepsilon$ on FBG sensor 4 (1560nm) simultaneously. Figure 14 shows that the four channels can be demodulated simultaneously. Note that the low frequency fluctuations seen in the signals are due to environmental noise-induced *intensity* fluctuations as explained earlier in this paper, and these can be removed using a balanced detection scheme if necessary. Also note that although the applied signal amplitude for all four channels are the same, the demodulated signal amplitude for each channel is different. This is mainly due to the fact that each channel has different optical intensity (due to non-uniform EDFA gain). In practice, this can either be pre-calibrated, or a gain-flattened EDFA can be used.
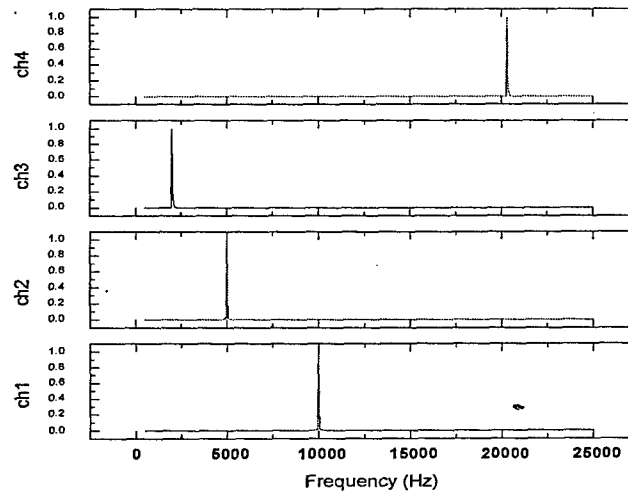
Figure 15 Fourier spectrum of the four-channel TWM wavelength demodulated signal shown in Figure 14. There is no detectable crosstalk between these four channels.

The crosstalk between these four channels can be inferred from the Fourier spectra of the signals shown in Figure 14. If there were crosstalk, we would expect all the frequency components, namely 2 kHz, 5 kHz, 10 kHz and 20 kHz, to show up in the signal spectrum of each channel. Figure 15 is the Fourier spectrum of the four channel

signals. In the spectrum of channel 1, there is only the expected 10 kHz component and no other frequency components are observed. This is true also for the other three channels. It is safe to conclude that the crosstalk between these four channels is at most comparable to the noise level in the Fourier spectrum, which is at least 30dB below the signal level in our case.

III. References

1. C.S. Sun, and F. Ansari, "Design of the fiber optic distributed acoustic sensor based on Michelson interferometer and its location application," Optical Engineering **42**, 2987-2993 (2003).

2. J. Kiddy, C. Baldwin, T. Salter, T. Chen, "Structural load monitoring of RV Triton using Fiber Optic Sensors," in *Smart Structures and Materials: Industrial and Commercial Applications of Smart Structures Technologies*, Anna-Maria and R. McGowan, eds., Proc. SPIE **4698**,462-472 (2002).

3. R. O. Claus, *Fiber Optic Sensor Based Smart Materials and Structures* (Institute of Physics Publishing, PA 1992).

4. F. Ansari., *Fiber Optic Sensors for Construction Materials and Bridges* (Technomic Publishing Co., Lancaster, PA, 1998).

5. B. Culshaw, J. Dakin, *Optical Fiber Sensors: Applications, Analysis, and Future Trends* (Artech House Books, Boston, 1996).

6. E. Udd, *Fiber Optic Smart Structures* (John Wiley, New York, 1995)

7. Grattan and B.T. Meggitt, *Optical Fiber Sensing Technology* (Chapman, UK, 1995).

8. E.Udd, *Fiber Optic Sensors: An Introduction for Engineers and Scientists* (Wiley, New York, 1991).

9. R.O.Claus and C.D.Thompson , "Optical Fiber-Based Ultrasonic Wave Generation and Detection in Materials", in *Rev. Prog. QNDE, vol. 10B*, (Plenum press, New York 1991), pp. 360-369.

10. A.D. Kersey, T.A. Berkoff and W.W. Morey, "Multiplexed fiber Bragg grating strain-sensor system with a Fabry-Perot wavelength filter," Optics Letters **18**, 1370-1372 (1993).

11. M. Xu, G.H. Geiger and J.P. Dakin, "Modeling and performance analysis of a fiber Bragg grating interrogation system using an acousto-optic tunable filter," IEEE Journal of Lightwave Technology **14**, 391-396 (1993).

12. G.A. Ball, W.W. Morey, and P.K. Cheo "Fiber laser source/analyzer for Bragg-grating sensor array interrogation," IEEE Journal of Lightwave Technology **12**, 700-703 (1994).

13. P. Fomitchov and S. Krishnaswamy, "Response of a Fiber Bragg-Grating Ultrasound Sensor," Optical Engineering **42**, 956-963 (2003).

14. I. Perez, H. Cui and E. Udd, "Acoustic emission detection using Fiber Bragg Gratings," in Smart structures and materials, E. Udd and D. Inaudi, eds., Proc. SPIE **4328**, 209-215 (2001).

15. M.A. Davis and A.D. Kersey, "Application of a fiber Fourier Transform spectrometer to the detection of wavelength encoded signals from Bragg-grating sensors," IEEE Journal of Lightwave Technology **13**, 1289-1295 (1995).

16. A.D. Kersey, T.A. Berkoff, and W.W. Morey, "High resolution fiber-grating based strain sensor with interferometric wavelength shift detection," Electronics Letters **28**, 236-238 (1992).

17. L. Solymar, D.J. Webb, and A. Grunnet-Jepsen, *The Physics and Applications of Photorefractive Materials* (Clarendon Press, Oxford 1996).

18. M.P. Petrov, S.I. Stepanov, and A.V. Khomenko, *Photorefractive Crystals in Coherent Optical Systems* (Springer-Verlag, Berlin 1991).

19. R.K. Ing and J.P. Monchalin "Broadband optical detection of ultrasound by two-wave mixing in a photorefractive crystal," Appl. Phys. Lett. **59**, 3233-3235 (1991).

20. B.F. Pouet, R.K. Ing, S. Krishnaswamy and D. Royer, "Heterodyne interferometer with two-wave mixing in photorefractive crystals for ultrasound detection on rough surfaces," Appl. Phys. Lett. **69**, 3782-3784 (1996)

21. P. Delaye, A. Blouin, D. Drolet, L.A. Montmorillon, G. Roosen, and J.P. Monchalin, "Detection of ultrasonic motion of a scattering surface by photorefractive InP:Fe under an applied dc field," J. Opt. Soc. Am. B **14**, 1723-1734 (1997).

22. A. Blouin, D. Levesque, C. Neron, D. Drolet, And J.P. Monchalin, "Improved resolution and signal-to noise ratio in laser ultrasonics by SAFT processing" Optics Express **2**, 531-539 (1998)

23. H. Tuovinen and S. Krishnaswamy, "Directionally sensitive photorefractive interferometric line receiver for ultrasound detection on rough surfaces," Appl. Phys. Lett. **73**, 2236-2238 (1998).

24. U. Gubler, D. Wright, W.E. Moerner and M.B. Klein, "Photochromic polymers for the optical homodyne detection of ultrasonic surface displacements", Optics Letters **27**, 354-356 (2002).

25. D.D. Nolte, *Photorefractive effects and materials* (Kluwer Academic Publishers, Dordrecht, 1995).

26. T.W. Murray, H. Tuovinen, and S. Krishnaswamy, "Adaptive optical array receivers for Detection of Surface Acoustic Waves," Applied Optics **39**, 3276-3284 (2000).

27. T.W. Murray and S. Krishnaswamy, "Multiplexed Interferometer for Ultrasonic Imaging Applications," Optical Engineering **40**, 1321-1328 (2001).

28. P.F. Fomitchov, T.W. Murray and S. Krishnaswamy, " Intrinsic Fiber Optic Sensor Array using Multiplexed Two-wave Mixing Interferometry," Applied Optics **41**, 1262-1266 (2002).

29. A. Othonos, and K. Kalli, *Fiber Bragg Gratings* (Artech House, Boston, 1999).

30. G. Coppola, A. Minardo, A. Cusano, G. Breglio, G. Zeni, A. Cutolo, A. Calabro, M. Giordano and L. Nicolais, "Analysis of Feasibility on the use of fiber Bragg grating sensors as ultrasound detectors," in *Smart structures and materials*, E. Udd and D. Inaudi, eds., Proc. SPIE **4328**, 224-232 (2001).

31. A.A. Kamshilin and V.V. Prokofiev, "Fast adaptive interferometer with a photorefractive GaP crystal", Optics Letters **27**, 1711-1723 (2002).

32. T. Kume, K. Nonaka, M. Yamamoto, and S. Yagi, "Wavelength-multiplexed holographic data storage by use of reflection geometry with a cerium-doped strontium barium niobate single-crystal structure and a tunable laser diode," Applied Optics **37**, 334-339 (1998).

REPORT DOCUMENTATION PAGE		Form Approved OMB No. 0704-0188

The public reporting burden for this collection of information is estimated to average 1 hour per response, including the time for reviewing instructions, searching existing data sources, gathering and maintaining the data needed, and completing and reviewing the collection of information. Send comments regarding this burden estimate or any other aspect of this collection of information, including suggestions for reducing the burden, to Department of Defense, Washington Headquarters Services, Directorate for Information Operations and Reports (0704-0188), 1215 Jefferson Davis Highway, Suite 1204, Arlington, VA 22202-4302. Respondents should be aware that notwithstanding any other provision of law, no person shall be subject to any penalty for failing to comply with a collection of information if it does not display a currently valid OMB control number.
PLEASE DO NOT RETURN YOUR FORM TO THE ABOVE ADDRESS.

1. REPORT DATE (DD-MM-YYYY) 28-03-2006	2. REPORT TYPE Technical Report	3. DATES COVERED (From - To) Sep 2005 - Dec 2006

4. TITLE AND SUBTITLE Low-Cost Adaptive Array Demodulation of Bragg-Grating and Interferometric Sensors for Health Monitoring of Marine Structures	5a. CONTRACT NUMBER
	5b. GRANT NUMBER N00014-04-1-0052
	5c. PROGRAM ELEMENT NUMBER
6. AUTHOR(S) Sridhar Krishnaswamy Yi Qiao Yi Zhou	5d. PROJECT NUMBER
	5e. TASK NUMBER
	5f. WORK UNIT NUMBER

7. PERFORMING ORGANIZATION NAME(S) AND ADDRESS(ES) Northwestern University Office of Research 633 Clark Street, Rm 2-502 Evanston, IL 60208	8. PERFORMING ORGANIZATION REPORT NUMBER

9. SPONSORING/MONITORING AGENCY NAME(S) AND ADDRESS(ES) Office of Naval Research 875 N. Randolph St. One Liberty Center Arlington, VA 22203-1995	10. SPONSOR/MONITOR'S ACRONYM(S) ONR
	11. SPONSOR/MONITOR'S REPORT NUMBER(S)

12. DISTRIBUTION/AVAILABILITY STATEMENT

Approved for Public Release; distribution is Unlimited

13. SUPPLEMENTARY NOTES

14. ABSTRACT

We have demonstrated a novel two-wave mixing (TWM) wavelength demodulation scheme for FBG sensors that has the ability to compensate for quasistatic drifts without the need for active stabilization. This method is suitable for measuring dynamic and transient strains such as those induced by vibrations, impact, ultrasound, or acoustic emission. Furthermore, this scheme can be readily multiplexed by using wavelength division multiplexing. Thus far, a four-channel TWM device has been demonstrated to demodulate dynamic strain signals from four FBG sensors simultaneously.

15. SUBJECT TERMS

Fiber Bragg Grating sensors; acoustic emission sensors; structural health monitoring

16. SECURITY CLASSIFICATION OF:			17. LIMITATION OF ABSTRACT	18. NUMBER OF PAGES	19a. NAME OF RESPONSIBLE PERSON Sridhar Krishnaswamy
a. REPORT	b. ABSTRACT	c. THIS PAGE			19b. TELEPHONE NUMBER (Include area code) 847-491-4006

Standard Form 298 (Rev. 8/98)
Prescribed by ANSI Std. Z39.18